Measurement of bubble sizes in fluidised beds using electrical capacitance tomography

CrossMark

T.C. Chandrasekera, Y. Li [1], D. Moody, M.A. Schnellmann, J.S. Dennis, D.J. Holland [*,2]

Department of Chemical Engineering and Biotechnology, University of Cambridge, New Museums, Pembroke Street, CB2 3RA, Cambridge, United Kingdom

HIGHLIGHTS

- Electrical capacitance tomography (ECT) is used to characterise a fluidised bed.
- Here, ECT measurements are reconstructed by penalising the Total Variation.
- Algorithm permits characterisation of regions with sharp changes in permittivity.
- ECT measurements of the bubble size are compared with existing correlations.

ARTICLE INFO

ABSTRACT

Electrical capacitance tomography (ECT) provides a means for non-invasively imaging multiphase flows, such as those in fluidised beds. Traditionally ECT images are reconstructed using the assumption that the distribution of permittivity varies smoothly throughout the sensor region. However, for many applications there are step changes in the permittivity, for example, between the bubble and particulate phases in a fluidised bed, and the assumption of smoothness is flawed. In this article a Total Variation Iterative Soft Thresholding (TV-IST) algorithm is used to reconstruct ECT images that allows for sharp transitions in the permittivity distribution. This new algorithm has been compared with established algorithms for ECT image reconstruction. It was found that the TV-IST algorithm reduced the sensitivity to the threshold level chosen when extracting measurements of bubble size from ECT data sets. Measurements of the bubble size distribution in the fluidised bed using the TV-IST algorithm agreed closely with established empirical correlations for the size of bubbles. The results demonstrate that ECT can provide accurate and high spatial resolution measurements of features such as bubbles in gas-solid fluidised beds.

1. Introduction

Gas-solid fluidised beds are widely used in industry in applications ranging from energy and petrochemicals to pharmaceuticals and food processing. Despite their widespread use, many fundamental phenomena in fluidised beds are poorly understood. For example, there is still debate about how best to estimate the rise velocity of bubbles (Müller et al., 2007a). A major reason for this uncertainty is that fluidised beds are opaque, making experimental observations challenging. Electrical capacitance tomography (ECT) is a non-invasive technique with the potential to characterise the bubble size and shape in three-dimensional fluidised beds.

ECT is fast, cheap and flexible and so it should be possible to study fluidised beds across a range of length scales. For these reasons ECT has been used by a number of researchers to study the dynamics of fluidised beds (e.g. Chandrasekera et al., 2012b; Du et al., 2006, 2005; Dyakowski et al., 2000; Halow, 1995; Holland et al., 2009; Makkawi and Wright, 2004, 2002; Pore et al., 2012; Wang et al., 1995, 2006). However, quantification of structures using ECT is challenging because the distribution of permittivity in the reconstructed images is assumed to vary smoothly. In this article, an image reconstruction algorithm is introduced permitting sharp transitions between regions of relatively constant permittivity. This new algorithm is demonstrated to improve the resolution of features such as bubbles in gas-solid bubbling fluidised beds.

ECT consists of placing an array of electrodes around the outside of a containing vessel and measuring the capacitance induced on these electrodes when a voltage is applied to each electrode in turn. The capacitance is related to the distribution of permittivity through the potential field within the space enclosed by the sensor. Therefore, the distribution of the permittivity can be recovered by solving

* Corresponding author.
E-mail address: djh79@cam.ac.uk (D.J. Holland).
[1] Now at the Ocean Science & Technology Division, Graduate School at Shenzhen, Tsinghua University, China.
[2] Now at the Department of Chemical and Process Engineering, University of Canterbury, Christchurch, New Zealand.

the inverse problem characterised by the measured capacitance and the potential field. Image reconstruction in ECT is complicated by three major factors. (i) ECT is a soft field technique, meaning that the path over which the measurements are sensitive is both non-linear and dependent on the permittivity distribution within the sensor. (ii) The ECT reconstruction problem is ill-conditioned meaning that the reconstructed image is very sensitive to noise in the measurements of capacitance. (iii) The ECT reconstruction problem is ill-posed because vastly fewer measurements are obtained than there are pixels in the final image. In a typical sensor, there will be 12 electrodes giving 66 independent measurements. The final image will be reconstructed with say 64×64 pixels, meaning that the problem is under-determined by a factor of approximately 50 (assuming a circular sensor). All three of these factors limit the quality of the results obtained from conventional reconstruction techniques.

Image reconstruction in ECT was initially performed using linear back projection (LBP); however, this is known to yield images of poor quality and with low resolution (Yang and Peng, 2003). More advanced algorithms were quickly adapted to ECT including the algebraic reconstruction technique (ART) (Reinecke and Mewes, 1996), simultaneous iterative reconstruction technique (SIRT) (Bangliang et al., 2000), projected Landweber iteration (PLI) (Yang et al., 1999), and Tikhonov regularisation (Peng et al., 2000). These algorithms effectively reconstruct the image using an l_2-norm penalty term, which is defined as the square root of the sum of the squared voxel-intensity values in the image. The l_2-norm permits robust reconstruction even in the presence of noise. However, the l_2-norm penalty results in excessively-smoothed images and prevents reproduction of the sharp transitions characteristic of bubbles in fluidised beds, seen, for example, by magnetic resonance imaging (Müller et al., 2007c). Other algorithms incorporating additional penalty terms have been proposed (Warsito and Fan, 2001); however, these still tend to be dominated by a smoothness criterion.

An alternative approach to image reconstruction is to use the l_1-norm. The l_1-norm has attracted considerable interest in recent years through its ability to accurately reconstruct images from heavily undersampled data, provided that the images can be represented sparsely in some domain. These ideas have strong connections to image compression and form the basis of the concept known as compressed sensing (or compressive sensing) (Candès et al., 2006; Donoho, 2006). The formal derivations of compressed sensing do not hold for ECT owing to factors (i) and (ii) described above. However, an l_1-norm penalty function can be introduced. One example of an l_1-norm penalty is the so called "Total Variation". Total Variation is essentially the sum of the absolute values of the gradient of an image. Reconstruction techniques which penalise the "total variation" of the image intensity have been shown to produce reasonable images of physical systems where there are sharp transitions in intensity (Fang, 2004; Soleimani and Lionheart, 2005).

In this article, a simple and efficient iterative soft thresholding algorithm is introduced to reconstruct ECT images by penalising the Total Variation of the image. The algorithm is shown to be highly robust and to enable the reconstruction of sharp boundaries in the final image using both simulated and experimental phantoms. ECT is then used to measure the size of bubbles in a freely-bubbling fluidised bed. The resulting bubble size distributions are compared with those predicted by the correlations of Darton et al. (1977), Rowe (1976) and Werther (1977).

2. Image reconstruction method

2.1. Background to electrical capacitance tomography

In ECT, an array of N electrodes is placed around the outside of a vessel or pipe. An a.c. voltage is applied across a pair of electrodes

and the resulting capacitance is measured. The capacitance for the ith pair of electrodes, C_i, is a function of the permittivity distribution, as given by

$$C_i = -\frac{1}{V_i} \iint_{S_i} \varepsilon(x,y) \nabla \varphi(x,y) dS_i \qquad (1)$$

where $\varepsilon(x,y)$ is the permittivity distribution, V_i is the potential difference between the two electrodes, $\phi(x,y)$ is the potential field distribution and S_i is the electrode surface. However, the capacitance is a non-linear function of the permittivity because the potential field is also affected by changes in the distribution of permittivity within the sensor, hence ECT is regarded as a soft field technique. In order to reconstruct $\varepsilon(x,y)$ it is necessary to account for changes in both the permittivity and potential. This can be approximated by assuming that changes in permittivity, $\Delta\varepsilon$, are small and that the map of permittivity can be discretised. Therefore, a Taylor series expansion of Eq. (1) for small discrete changes gives:

$$\Delta C_i = \sum_{j=1}^{n} s_{ij} \Delta\varepsilon_j \qquad (2)$$

where $s_{ij} = \partial C_i/\partial\varepsilon_j$ are the elements of a matrix describing the change in the capacitance between the ith pair of electrodes obtained when there is a small change in the permittivity $\Delta\varepsilon_j$, at a given location (j). The location, j, corresponds to the spatial co-ordinates (x_j, y_j). By measuring the capacitance between all pairs of electrodes, a set of linear equations can be obtained relating the capacitance and the permittivity. It is then possible to obtain a map of $\varepsilon(x,y)$ in the space contained within the electrodes by solving the inverse problem described by the set of Eq. (2). However, the map of permittivity will typically comprise a much larger number of pixels, n, than there are measurements, m. If the sensor is comprised of N electrodes, then the total number of independent measurements m is given by:

$$m = \frac{1}{2}N(N-1). \qquad (3)$$

A typical sensor will contain between 8 and 16 electrodes, yielding between 28 and 120 linearly-independent measurements. It is in solving this under-determined, linearised equation that concepts from compressed sensing can be applied.

2.2. Total variation iterative soft thresholding

Conventional techniques for iterative reconstruction, such as the versions of ART, SIRT and the bound-projected version of the Landweber iteration implemented by Hansen and Saxild-Hansen (2012), are well suited to recovering images from ECT, provided there are no sharp changes in intensity. However, many images contain sharp changes in intensity, such as the bubbles seen in gas-solid fluidised beds. This case requires an alternative approach. Compressed sensing theory predicts that accurate reconstructions of images from under-determined systems of linear equations can be found, provided that the resultant image can be represented sparsely in some domain. In the case of systems with sharp transitions in intensity, such as gas bubbles in a fluidised bed, the spatial gradients of the image represent the image sparsely. Here, an algorithm is proposed that reconstructs ECT data sets by penalising the l_1-norm of the spatial finite difference of the image, otherwise known as the total variation of the image. The method of solution was derived from the iterative thresholding algorithms commonly used in compressed sensing (Tropp and Wright, 2010). The method builds on previously published approaches used for image restoration of blurred and noisy photographic images (Beck and Teboulle, 2009a, 2009b; Michailovich, 2011; Wang et al., 2008). A full description of the algorithm has been published elsewhere (Chandrasekera et al., 2012a), therefore only a brief summary of the most pertinent features of the algorithm is given here.

The 2D image, $f(x,y)$ of normalised permittivity values is stored as a column vector, $\mathbf{f}$ in which each element corresponds to a pixel (x,y) in the imaging region. In total, f has n elements, corresponding to the number of pixels in the (circular) imaging region. The gradient of the image is represented by two column vectors (each of length n), $\mathbf{g_x}$ and $\mathbf{g_y}$, corresponding to the horizontal and vertical finite differences of the image, respectively. The 'inverse' transform from gradient to image requires the assumption that the image is zero outside of the imaging region and the solution of a least-squares problem (Michailovich, 2011).

The total variation, TV, is defined as

$$\mathrm{TV} = \|\sqrt{\mathbf{g_x}^T\mathbf{g_x}+\mathbf{g_y}^T\mathbf{g_y}}\|_1 = \sum_{i=1}^{n}\left(\left(g_x(i)\right)^2+\left(g_y(i)\right)^2\right)^{0.5}, \qquad (4)$$

where $g_x(i)$ and $g_y(i)$ correspond to the ith element of the vectors $\mathbf{g_x}$ and $\mathbf{g_y}$. The total variation defined by Eq. (4) corresponds to the isotropic total variation; anisotropic total variation is an alternative definition whereby the summation is over the absolute values of the gradient-components in each direction.

The reconstruction problem in terms of the image gradient is thus

$$\min_{\mathbf{g_x},\mathbf{g_y}}\left[\|\mathbf{c}-\mathbf{Kf}\|_2^2+\alpha\|\sqrt{\mathbf{g_x}^T\mathbf{g_x}+\mathbf{g_y}^T\mathbf{g_y}}\|_1\right], \qquad (5)$$

where $\mathbf{c}$ is the column vector (length m) of capacitance measurements, $\mathbf{K}$ is the $m \times n$ sensitivity matrix, the image $\mathbf{f}$ is obtained from the gradient field ($\mathbf{g_x}$ and $\mathbf{g_y}$), and α is a trade-off parameter that controls the extent of total variation penalisation. In the case of $\alpha=0$, Eq. (5) corresponds to a least-squares fit of the gradient field to the capacitance measurements. The optimisation in Eq. (5) was performed by the Fast Iterative Shrinkage-Thresholding Algorithm (FISTA) (Beck and Teboulle, 2009a).

In summary, the TV-IST algorithm estimates the gradient of the image to fit the capacitance measurements, subject to the prior knowledge that the gradient is sparse, over a fixed number of iterations, $k_{\max}$. The contribution of the prior knowledge is controlled by the threshold parameter, α. Complete details of the algorithm are given elsewhere (Chandrasekera et al., 2012a).

3. Experimental

The capacitance sensor used in this work used 12 electrodes placed evenly around a circular pipe. A schematic diagram of the sensor is shown in Fig. 1. The sensor consisted of a PEEK pipe (relative permittivity ε_r 3.4) of length 300 mm, thickness 5 mm and internal diameter 50 mm. The 12 electrodes, each 70 mm in vertical height and 10 mm in length around the arc with a 1.5 mm insulation gap and 1.66 mm earth between each electrode, were spaced evenly around the outside of the PEEK pipe. Experimental capacitance measurements were acquired using the M3c ECT system (Industrial Tomography Systems). The signal to noise ratio (SNR) for these measurements was typically around 65 dB. Two experimental systems were studied. Firstly, a tube filled with particles of silica-alumina catalyst support was imaged to test the accuracy of the TV-IST algorithm on a static system. The outer diameter of the tube was 20 mm and the wall thickness was 3 mm. The tube was located slightly off-centre within a 50 mm inner diameter sensor because if the system is symmetric within the sensor the image is simpler to reconstruct. For this apparatus, capacitance measurements for calibration were acquired for the sensor filled with silica-alumina catalyst support ($\varepsilon_r \approx 3$) and separately with only air in the sensor. Secondly, a fluidised bed was imaged, the arrangement being shown schematically in Fig. 2. The bed was constructed from polymethyl methacrylate and had an inner diameter of 50 mm. Lobelia seeds (experimentally-measured
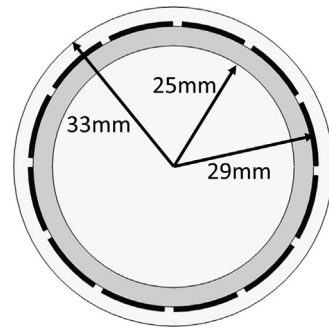

Fig. 1. Schematic illustration of the ECT sensor. The electrodes are indicated by the solid black lines, the pipe wall is indicated by the darker grey region. The electrodes are surrounded by a guard electrode of radius 33 mm. The material to be imaged is contained within the central region of radius 25 mm.
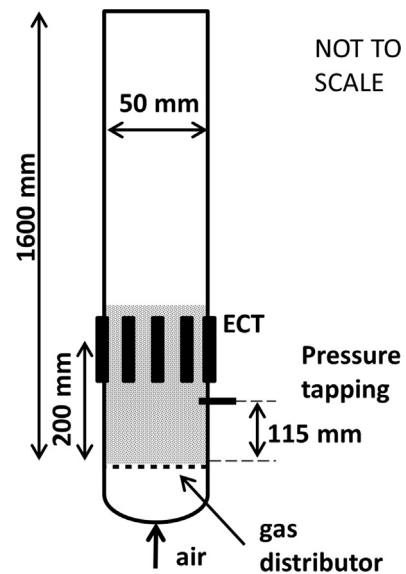

Fig. 2. Schematic illustration of the fluidised bed used for the experimental measurement of the bubble size. The settled bed height was 385 mm. The particles were lobelia seeds 0.3 mm in diameter. Air was supplied at 298 K and 1 barg at flow rates between 110 and 180 cm^{3}s^{-1}.

minimum fluidisation velocity with air at 298 K and 1 bara $U_{\mathrm{mf}}=0.05$ m s^{-1}, particle diameter $d_p=0.3$ mm, density $\rho_p=1000$ kg m^{-3}) were used as the medium fluidised. The settled bed height was 385 mm. ECT images are typically obtained from normalised capacitance data, which require measurements of the capacitance with the sensor filled with a high permittivity and low permittivity material (Xie et al., 1992). The high calibration measurement was obtained by filling the bed with unfluidised seeds. The low calibration was obtained using air. The high and low calibration measurements indicated that a SNR of 65 dB for the raw capacitance measurement corresponded to a peak SNR of approximately 34 dB based on the change in capacitance. The twelve-electrode ECT sensor was modelled using the finite element method in the Comsol Multiphysics software package. The $m \times n$ sensitivity matrix ($\mathbf{K}$) was generated in MATLAB using the output from Comsol.

ECT images were reconstructed using LBP, PLI, ART (relaxed Kaczmarz iteration), SIRT (relaxed Cimmino iteration) and the TV-IST algorithm. All reconstructions were performed on a standard laptop PC with a 2.2 GHz Intel Core2 Duo processor and 4 GB RAM. The conventional iterative algorithms were implemented using the MATLAB toolbox developed by Hansen and Saxild-Hansen (2012): 100 iterations were used throughout for each of these algorithms; the

projected versions of these algorithms were used to constrain the images to be non-negative. The TV-IST algorithm was implemented in MATLAB and run for each set of capacitance measurements with 500 iterations (taking approximately 30 s to complete per image).

4. Results

In this section, the accuracy and resolution achieved using the TV-IST algorithm was examined and compared with conventional LBP, PLI, ART and SIRT reconstruction techniques using determinations of capacitance predicted by a finite-element simulation. The algorithm was then used to reconstruct images based on experimental measurements of the simple phantoms, and, finally, was used to measure bubble sizes in the fluidised bed.

4.1. Numerical simulations of the ECT measurement

To demonstrate the validity of the TV-IST image reconstruction algorithm, Comsol was used to simulate the capacitance that would be obtained for a number of simple phantoms. Fig. 3(a) shows a phantom consisting of a circular object placed in the centre of the sensor cross-section alongside reconstructions of this phantom using (b) LBP, (c) PLI, (d) ART, (e) SIRT and (f) the new TV-IST (with threshold parameter α, as defined in Eq. (5), set to 9×10^{-5}) algorithm. The relative permittivity of the cylindrical wall and circular object were set to 3.3 and 2.1, respectively, in the simulation. Both the sensitivity matrix and capacitance measurements were calculated using Comsol with 12 electrodes spaced evenly around the outside of the cylindrical wall shown in Fig. 3(a), providing 66 independent simulated capacitance measurements. Gaussian-distributed noise was added to the simulated measurements such that the peak signal-to-noise ratio in the measurements was 34 dB. In all cases, the reconstruction was performed using the linearised change in capacitance for measurements through the cylindrical wall of thickness five pixels, i.e. the normalised capacitance included the cylindrical boundary. The normalised capacitance was used to help minimise the effect of non-linearity introduced by the wall of the sensor (Yang et al., 1999). Only the region within the wall (i.e. not including the wall) was reconstructed and therefore the wall is not seen in the reconstructed images. The central region reconstructed was identified as those pixels within a radius of 25 pixels from the centre of the image.
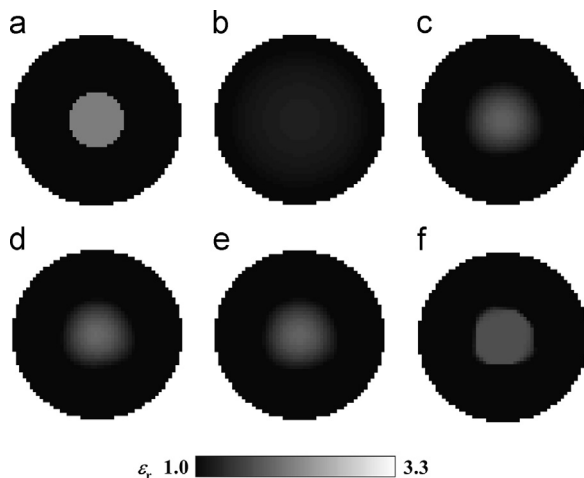
A quantitative measure of the accuracy of the reconstruction was obtained by calculating a relative root mean squared error as follows:

$$\text{relative root mean squared error} = \left(\frac{\sum\limits_{i=1}^{n} \left(\varepsilon_{\text{phantom}}(i) - \varepsilon_{\text{reconstruction}}(i) \right)^2}{\sum\limits_{i=1}^{n} \left(\varepsilon_{\text{phantom}}(i) \right)^2} \right)^{0.5}$$

(6)

Fig. 3(b) shows that the circular shape of the central object can be recovered by the LBP reconstruction, but it is significantly smoothed and broadened in comparison with the true image in Fig. 3(a) and consequently the intensity is reduced. The PLI, ART and SIRT results in Fig. 3(c-e) are all similar and recover the size of the circular object, but with higher intensity than expected in the centre of the object and lower intensity at the edge. The smooth variation in the permittivity distribution shown in Fig. 3(b-e) makes precise identification of the boundary of the object challenging. An approximate quantitative comparison of the quality of the reconstructed images is given by the relative root mean squared error shown in Table 1. The relative root mean squared error for the LBP reconstruction is 0.113, which is high as expected. The relative mean squared error for the PLI, ART and SIRT are all between 0.065 and 0.069. This further indicates a substantial reduction in error when compared with the LBP reconstructions, although it also indicates that the results with all three techniques are quite similar. Further discussion will therefore focus on the comparison between PLI and TV-IST.

The TV-IST result of Fig. 3(f) shows a uniform intensity across the central object, consistent with the true distribution shown in Fig. 3(a). However, the estimated relative permittivity value in Fig. 3(f) was 1.7, which is lower than the value of 2.1 for the phantom shown in Fig. 3(a). The lower permittivity may be related to the noise in the simulated measurements, or to the suppression of intensity inherent in l_1-minimisation algorithms, such as iterative soft thresholding. The permittivity at the edges of the object jumps sharply for the TV-IST case, whereas for the PLI image shown in Fig. 3(c) a gradual transition in permittivity is observed. The relative root mean squared error for the TV-IST reconstruction was 0.061, which is lower than for any of the other reconstructions. These results demonstrate that the TV-IST algorithm can produce sharper images, with lower total error than conventional image reconstruction algorithms.

Fig. 4(a) is a simulated phantom with two circles, both of relative permittivity 1.0, but of different size. These circles are surrounded by material with relative permittivity 3.2. Note that the colour scale has been inverted for these images. As with the single circle case, shown in Fig. 3, the phantom includes the circular wall with relative permittivity 3.3, although the wall is not seen in the Figure because the normalised capacitance was used for the calculations. The capacitance measurements were theoretically simulated using Comsol and noise was added to give a peak signal-to-noise ratio of 34 dB for the normalised capacitance. As is well established, LBP gives poor results and the PLI, ART and SIRT all yield similar permittivity distributions, therefore Fig. 4 only shows the PLI and TV-IST results. Fig. 4(b) shows that the PLI

Fig. 3. Simulation illustrating ECT reconstruction of a phantom consisting of a single circular region with a relative permittivity of 2.2. The capacitance measurements for this simulation were calculated using Comsol with Gaussian noise added such that the signal-to-noise ratio was 34 dB. (a) The original phantom image. Reconstructions of the phantom are shown for (b) LBP, (c) PLI, (d) ART, (e) SIRT, (f) TV-IST.

Table 1
Relative errors corresponding to the results in Fig. 3.

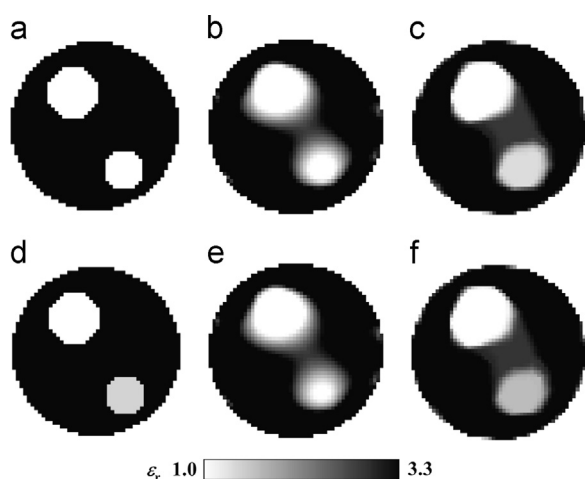| Reconstruction method	Relative root mean squared error
Linear back projection (LBP)	0.113
Projected landweber iteration (PLI)	0.069
Algebraic reconstruction technique (ART)	0.065
Simultaneous iterative reconstruction technique (SIRT)	0.067
Total variation iterative soft thresholding (TV-IST)	0.061

Fig. 4. Simulation illustrating ECT reconstruction of a two-void phantom, surrounded by material with a relative permittivity of 3.2. The capacitance measurements for this simulation were calculated using Comsol with Gaussian noise added such that the signal-to-noise ratio was 34 dB. (a) The original phantom image. Reconstructions of the phantom are shown for (b) PLI, (c) TV-IST. (d) phantom with relative permittivity in the smaller void increased to 1.2. Reconstruction of (d) using (e) PLI and (f) TV-IST.

method clearly distinguishes the two objects; however, the boundary of each object is smooth with no sharp transition from the region of low permittivity to that of high permittivity. Fig. 4(c) shows the TV-IST reconstruction of the same simulated capacitance data. Again, the two objects are well resolved, but in this case the boundary surrounding each object is sharper. There is some distortion in the circular shape of the objects and a low intensity "bridge" is formed between the two objects. The observed intensity within the smaller (bottom-right) void in Fig. 4(c) corresponds to an apparent relative permittivity of ∼1.3. Although the apparent relative permittivity is higher than the expected value of 1.0, the sharp transition of the TV-IST reconstruction makes demarcation of the boundary of the voids much simpler than in the case of the PLI reconstruction. The smooth transition in the permittivity of the PLI reconstruction means that a small change in the intensity level chosen to define the boundary of the void would result in a large change in the shape of the void. ECT is inherently a low resolution technique; the limited resolution manifests differently for different reconstruction algorithms. Thus, l_1-penalisation by total variation (TV-IST) yields a different artefact to the l_2-smoothing associated with the common iterative methods. Importantly, the distortion seen with the TV-IST algorithm is of a flat nature and therefore the outer boundary of the objects can be more readily identified than in the case of PLI, or other l_2-penalised algorithms.

To illustrate further the different artefacts arising in reconstructing these ECT images, the effect of a change in permittivity has been considered on the reconstruction. Fig. 4(d) shows a similar phantom to that seen in Fig. 4(a), except that the relative permittivity of the smaller void has been increased from 1.0 to 1.2. This value of 1.2 corresponds approximately to the void (relative permittivity 1.0) containing 10% vol. of material of relative permittivity 3.2. This object represents a gas bubble containing 10% vol. solids, for example. The capacitance measurements were simulated by adding noise to the values calculated with Comsol to give a peak-signal-to-noise ratio of 34 dB as before. Fig. 4(e) and (f) show reconstructions of Fig. 4(d) using PLI and TV-IST, respectively. The results are similar to those shown in Fig. 4(a-c). Both PLI and TV-IST reconstructions can distinguish between the two voids, and both reconstructions show a region of low permittivity connecting the two voids. In the case of PLI, the transition from low permittivity to high permittivity is smooth, as expected. By contrast, TV-IST shows an almost constant intensity within the two void regions and a sharp

transition to the region of high permittivity surrounding the voids. This difference is further exemplified when considering the permittivity and size of the reconstructed objects in Fig. 4(e) and (f). As noted above, the phantom in Fig. 4(d) is identical to that shown in Fig. 4(a), except that the relative permittivity in the smaller void is increased from 1.0 to 1.2. The reconstructions shown in Fig. 4(e) and (f) are similar to those shown in Fig. 4(b) and (c). However in the case of the PLI reconstruction shown in Fig. 4(e), the increase in permittivity has led to an apparent decrease in the diameter of the void from 11 mm to 8 mm, assuming that the void is identified as being any voxel with a relative permittivity of 1.5 or lower. This decrease in the diameter of the void stems from the difficulty in accurately identifying the appropriate intensity level to demarcate the two voids. In the case of the TV-IST algorithm, the size and shape of the smaller void is similar in both Fig. 4(c) and (f), even though the relative permittivity has increased from 1.3 to 1.5. Thus, the change in permittivity in the phantom is recovered by the PLI algorithm as a change in size of the object, whereas the TV-IST algorithm correctly identifies that the permittivity has increased in the smaller object, whilst the size and shape remains unchanged.

These results demonstrate that the TV-IST algorithm is capable of reconstructing ECT measurements with sharp transitions between regions of high and low permittivity. From the resulting images of the permittivity, the shape and size of voids or inclusions can be estimated readily, with little sensitivity to the threshold parameter (α). ECT measurements reconstructed using TV-IST are therefore promising as a technique for studying the bubble size and shape in, for example, gas-solid fluidised beds, considered later.

4.2. Experimental ECT measurements

Prior to demonstrating quantitative measurements of the bubble size in a fluidised bed, measurements of a simple experimental phantom were performed. The phantom consisted of a polymethyl methacrylate tube (relative permittivity 3.3) filled with dry silica-alumina catalyst support. Fig. 5 shows (a) a sketch of the phantom and (b) a reconstruction using the TV-IST algorithm (with threshold parameter α, as defined in Eq. (5), set to 1×10^{-3}) from the 66 capacitance measurements and the sensitivity matrix of the previous section. The filled tube is seen clearly in the image. It should be noted that the apparent relative permittivity is less than the expected value of ∼3 corresponding to random packing of these particles. The reduction in the apparent solid fraction is related to the contribution of the PEEK wall to the measurements, which is not modelled in the reconstruction, coupled with non-linear effects in the ECT reconstruction problem and the reduction in contrast inherent in l_1-regularisation methods, such as Eq. (5). However, the diameter of the observed circle is consistent with the 20 mm outer diameter of the tube. These results confirm that the TV-IST algorithm is effective at recovering the shape and size of objects obtained from experimental ECT measurements.
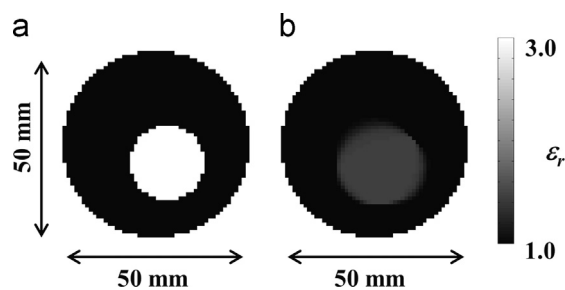

Fig. 5. (a) schematic illustration of the experimental rod phantom consisting of a single tube filled with silica-alumina particles. (b) ECT reconstruction of the phantom in (a) obtained from experimental measurements of the capacitance when using the TV-IST algorithm.

Experimental measurements of a gas-solid fluidised bed were performed using ECT with the projected Landweber iteration and the TV-IST algorithms. Fig. 6 gives some examples of a time series of images of bubbles in the fluidised bed at excess gas velocities of 0.008, 0.016 and 0.035 ms^{-1} reconstructed using the projected Landweber iteration algorithm. The images show the cross-section of bubbles within the fluidised bed. The apparent diameter of the bubbles increases and then decreases again as the bubbles pass through the sensor. These results are consistent with rising bubbles of approximately spherical or ellipsoidal shape. However, although it is clear that the ECT is able to track the passage of bubbles, as is well established, quantitative measurements of the bubble size using these results are challenging owing to the smooth variation in the intensity in the image. Fig. 7 shows ECT images reconstructed using the TV-IST algorithm for the same experimental measurements used to produce the images shown in Fig. 6. The general trends shown in Fig. 7 are very similar to those shown in Fig. 6; however the TV-IST reconstructions in Fig. 7 show much sharper transitions between regions of high and low permittivity. These images are consistent with high-resolution images obtained using magnetic resonance imaging (Müller et al., 2007c). As will be shown shortly, the sharp boundary exhibited between the regions of high and low permittivity means that quantitative analysis of the bubble size in fluidised beds using the TV-IST reconstructions is straightforward and robust.

Before examining the quantification of bubble size using TV-IST, it is important to consider the set-up of the algorithm. Algorithms such as TV-IST are sensitive to the correct choice of reconstruction parameters, in this case the value of the threshold parameter α, as defined by Eq. (5). Fig. 8 shows reconstructions of a single frame of the ECT measurements of the fluidised bed for different values of α. For all values of α shown, covering two orders of magnitude, two bubbles are seen, one at the top right and one at the centre left of the image. For smaller values of α, a region of low permittivity is also seen in the bottom right; this region resolves into a bubble-like

Fig. 7. Examples of ECT measurements reconstructed using the TV-IST algorithm for superficial gas velocities of 0.058 m s^{-1}, 0.066 m s^{-1}, and 0.085 m s^{-1}. Gas bubbles correspond to regions of low permittivity and are indicated by lighter colours. Images were obtained at 56 ms intervals, with every second image shown here. The diameter of the column was 50 mm.

shape when $\alpha=2\times10^{-4}$. However, it is unclear if this third region of low permittivity is a bubble or an artefact arising from noise in the measurements. Large values of α result in well-resolved objects, but the contrast between objects with different relative permittivity is low. Small values of α result in more artefacts remaining in the image, but keep relatively strong contrast between regions of high and low permittivity. The value of $\alpha=2\times10^{-4}$ represents a compromise between maximising the contrast in the image and minimising artefacts. The optimum value of α should be constant for a given ECT sensor and experimental system, however α would need to be optimised for different sensors, instruments and potentially when studying different fluidisation regimes. However, large structures in the fluidised bed will be recovered accurately for a wide range of choices of α.

ECT is inherently a low resolution technique, so prior to performing an extensive analysis of the bubble size measurements, it was important to verify that the ECT measurements were able to capture the majority of the bubbles in the fluidised bed. To do this, measurements of the pressure were obtained from the fluidised bed for the same experimental conditions as the ECT measurements shown above. Fig. 9 shows the major frequency of the fluctuations in the pressure. The frequency of pressure oscillations is indicative of the frequency of the passage of bubbles, for the fluidising conditions and particles used in the present work (Müller et al., 2007b). Determinations of the frequency of fluctuations from the raw experimental measurements of capacitance were also obtained for U - U_{mf} ranging from 0.008 m s^{-1} to 0.07 m s^{-1}, i.e. the maximum flow rate corresponds to 2.4 U_{mf}. Above this flow rate, large slugs were formed which filled the cross-section of the sensor. The frequency estimated from the ECT measurements was less than that measured by the pressure fluctuations, especially at an excess gas velocity of 0.008 m s^{-1}. For 0.01 m s$^{-1} < U$ - $U_{mf} < 0.05$ m s^{-1}, the ECT tends to measure a frequency approximately 0.4 Hz less than the pressure measurements. For U - $U_{mf} > 0.05$ m s^{-1}, the frequency measured by the ECT and
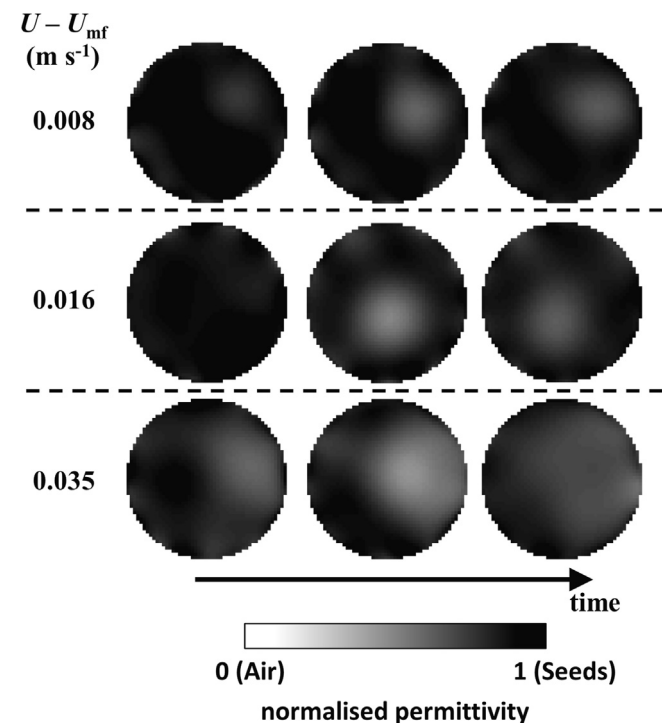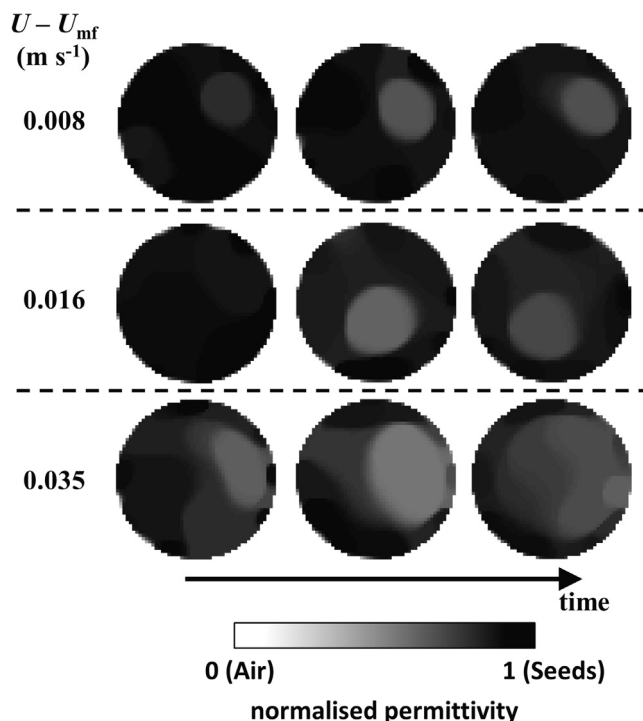

Fig. 6. Examples of ECT measurements reconstructed using PLI for excess gas velocities of 0.008 m s^{-1}, 0.016 m s^{-1}, and 0.035 m s^{-1}. Gas bubbles correspond to regions of low permittivity and are indicated by lighter colours. Images were obtained at 56 ms intervals, with every second image shown here. The diameter of the column was 50 mm.

pressure agree closely. The discrepancy at low gas velocities may be attributable to the ECT measurements not being able to identify all of the small bubbles present in this system or to coalescence of bubbles occurring between the pressure sensor and the ECT sensor. However, overall the agreement between the frequency measurements is good,

indicating that the ECT measurements are sufficiently sensitive to detect the passage of almost all bubbles under these flow conditions.

In order to estimate the diameters of the bubbles, ECT measurements from 11 s of acquisition were reconstructed using projected Landweber iteration and TV-IST for the entire range of gas
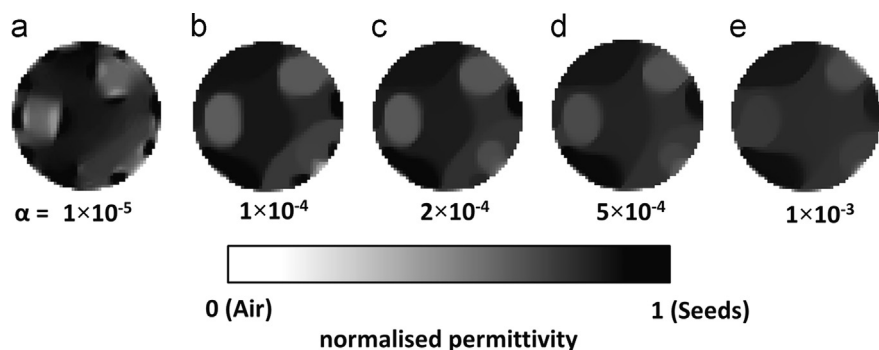

Fig. 8. Demonstration of the effect of the choice of the parameter α on the reconstructed image. Large values of α result in a strong loss of contrast, whilst small values of α are prone to artefacts. For values of α in the region of 2×10^{-4}, the reconstruction is not too sensitive to the choice of α and reasonable images are obtained.
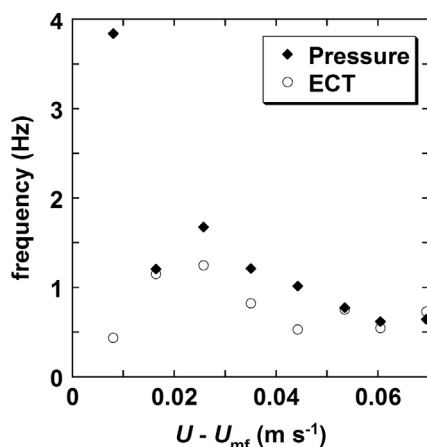

Fig. 9. Comparison of the frequency of measured fluctuations in the capacitance and pressure. Pressure measurements were acquired at a rate of 100 Hz and therefore can be used to test whether the ECT measurements are sufficiently fast to capture the major meso-scale phenomena occurring in the fluidised bed. The pressure measurements were obtained from a tapping 115 mm above the distributor, whilst the capacitance measurements were obtained from the ECT electrodes centred 200 mm above the distributor. For all excess gas velocities greater than 0.05 m s^{-1}, the fluctuations in the pressure and capacitance were equivalent, indicating that ECT measurements are sufficiently fast to characterise bubbles in the fluidised bed.
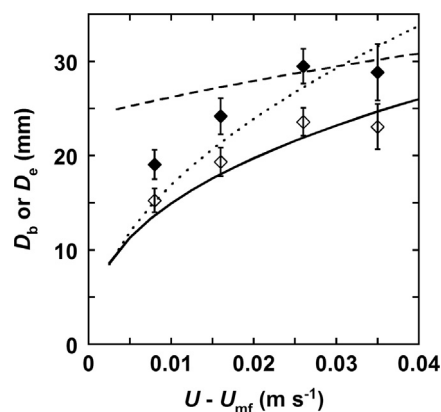

Fig. 11. Comparison of the bubble size distribution measured using ECT and the correlations of (–) Darton et al. (1977), (•••) Rowe (1976) and (- -) Werther (1977). Bubble sizes were calculated from (♦) the diameter of a circular bubble with equivalent cross-sectional area to the measured bubble D_b and (◇) the equivalent spherical diameter of a bubble with the same cross-sectional area, assuming that the bubble has a hemispherical shape, D_e. Bubble sizes were estimated from observations of at least five of the bubbles at each flow rate. The uncertainty in the bubble size was calculated as the standard deviation of the measured bubble sizes.
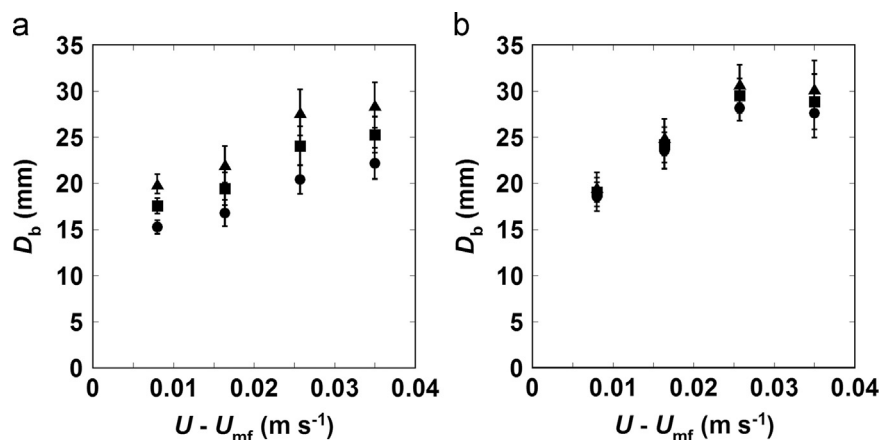

Fig. 10. Comparison of (a) PLI and (b) TV-IST for the characterisation of bubble size in a fluidised bed. The bubble size was estimated as the diameter of a circle of equivalent cross-sectional area to the measured bubble at its widest point. The error bars are given by the standard deviation of the measurements of at least five bubbles. Data are shown assuming a threshold of (•) 40%, (■) 50% and (▲) 60% of the maximum relative permittivity in each frame.

velocities studied. All of the frames for a particular flow rate were analysed and frames with clear bubbles were identified. Owing to the acquisition rate being 18 Hz, each bubble was detected three to four times as it passed through the bed. Therefore, for each bubble, the frame in which it appeared the largest was chosen to determine the diameter of the bubble. This frame should correspond most closely to the time at which the bubble is in the centre of the sensor. Since the bubbles were only rarely perfectly circular, the size of the bubble was calculated from the diameter of a circular bubble with equivalent cross-sectional area. The cross-sectional area was determined by choosing an intensity level for each image and setting all values above this value to black, indicating the particulate phase, and all values below this value to white, indicating the gas phase. A sensitivity analysis of the choice of the intensity level was performed by setting the value to be 0.4, 0.5 or 0.6 times the maximum change in the permittivity in each image. Fig. 10 shows a comparison of the bubble size measured using the projected Landweber iteration and TV-IST reconstructions. The uncertainty in the estimated bubble size is given by the standard deviation of the diameter of the bubbles measured. The apparent bubble size measured by both techniques is seen to increase with increasing excess gas velocity, as expected, and the estimated bubble size from both reconstruction techniques is approximately the same. However, the projected Landweber iteration shows significantly greater sensitivity of the estimated bubble to the choice of the intensity level used to identify bubbles. Changing the value of the intensity level from 0.4 to 0.6 times the maximum permittivity in the image increases the apparent bubble size in the projected Landweber iteration results by 5 mm to 10 mm, or approximately 30%, depending on the excess gas velocity. By contrast the TV-IST reconstructions are relatively insensitive to the chosen intensity level with the bubble size increasing by 1 mm to 2 mm, or approximately 5%, for the same change in the chosen intensity level. The decreased sensitivity of the reconstructions obtained using the TV-IST algorithm to the intensity level enables quantitative analysis of the bubble size to be performed with confidence.

To further demonstrate that the bubble size measurements performed using ECT with the TV-IST algorithm are quantitative, Fig. 11 shows a plot of the bubble size calculated from the TV-IST reconstructions for $U - U_{mf}$ ranging from 0.008 m s^{-1} up to 0.04 m s^{-1} alongside the expected bubble size obtained from the correlations of Darton et al. (1977), Rowe (1976) and Werther (1977). In this case, the bubble size was calculated as the diameter of a circular bubble with equivalent cross-sectional area, D_b, and the equivalent spherical diameter of a hemispherical bubble with the same cross-sectional area, D_e. The uncertainty in the measured bubble size is given by the standard deviation of the diameter of the bubbles measured. There is some discrepancy between the bubble sizes estimated from the correlations; however, the ECT measurements show excellent agreement with the correlations, lying within the range of all three correlations. If a hemispherical bubble is assumed, the diameter is in excellent agreement with the correlation of Darton et al. (1977).

5. Conclusions

A Total Variation Iterative Soft Thresholding (TV-IST) algorithm for the reconstruction of images obtained from ECT measurements has been presented. The new algorithm penalises the l_1-norm of the spatial finite differences of the image, viz. the total variation, using an iterative thresholding approach. The algorithm was demonstrated on simulated permittivity distributions, an experimental phantom and experimental measurements on a fluidised bed. The advantage of using the total variation penalty is that it accounts for sharp transitions between regions of high and low permittivity. The new algorithm was shown to provide a substantial improvement in the demarcation of the boundary between regions of high and low

permittivity within the fluidised bed. The enhanced identification of regions of high and low permittivity allows realistic quantitative measurements to be made of the size of features such as gas bubbles within a gas-solid fluidised bed. The experimental measurements on the fluidised bed demonstrated that the TV-IST algorithm is able to capture the size of gas bubbles in a fluidised bed accurately, with the experiments showing excellent agreement with existing correlations for the bubble size in a gas-solid fluidised bed, especially that of Darton et al. (1977).

References

Bangliang, S., Yiheng, Z., Lihui, P., Danya, Y., Baofen, Z., 2000. The use of simultaneous iterative reconstruction technique for electrical capacitance tomography. Chem. Eng. J. 77, 37–41.

Beck, A., Teboulle, M., 2009a. A fast iterative shrinkage-thresholding algorithm for linear inverse problems. SIAM J. Imaging Sci 2, 183–202.

Beck, A., Teboulle, M., 2009b. Fast gradient-based algorithms for constrained total variation image denoising and deblurring problems. IEEE Trans. Image Process 18, 2419–2434. http://dx.doi.org/10.1109/TIP.2009.2028250.

Chandrasekera, T.C., Li, Y., Dennis, J.S., Holland, D.J., 2012a. Total variation image reconstruction for electrical capacitance tomography. IEEE Imaging Systems and Techniques. Manchester, 584–589.

Chandrasekera, T.C., Wang, A., Holland, D.J., Marashdeh, Q., Pore, M., Wang, F., Sederman, A.J., Fan, L.S., Gladden, L.F., Dennis, J.S., 2012b. A comparison of magnetic resonance imaging and electrical capacitance tomography: an air jet through a bed of particles. Powder Technol. 227, 86–95.

Darton, R.C., La Nauze, R.D., Davidson, J., Harrison, D., 1977. Bubble growth due to coalescence in fluidised beds. Trans. Inst. Chem. Eng. 55, 274.

Du, B., Warsito, W., Fan, L., 2005. ECT studies of gas-solid fluidised beds of different diameters. Ind. Eng. Chem. Res. 44, 5020–5030.

Du, B., Warsito, W., Fan, L., 2006. Imaging the choking transition in gas-solid risers using electrical capacitance tomography. Ind. Eng. Chem. Res. 45, 5384–5395.

Dyakowski, T., Jeanmeure, L.F.C., Jaworski, A.J., 2000. Applications of electrical tomography for gas – solids and liquid – solids flows – a review. Powder Technol. 112, 174–192.

Fang, W., 2004. A nonlinear image reconstruction algorithm for electrical capacitance tomography. Meas. Sci. Technol. 15, 2124–2132. http://dx.doi.org/10.1088/0957-0233/15/10/023.

Halow, J.S., 1995. Capacitance imaging of fluidized beds. In: Williams, R.A., Beck, M.S. (Eds.), Process Tomography: Principles, Techniques and Applications. Butterworth Heinemann.

Hansen, P.C., Saxild-Hansen, M., 2012. AIR tools — A MATLAB package of algebraic iterative reconstruction methods. J. Comput. Appl. Math. 236, 2167–2178. http://dx.doi.org/10.1016/j.cam.2011.09.039.

Holland, D.J., Marashdeh, Q., Müller, C.R., Wang, F., Dennis, J.S., Fan, L.-S., Gladden, L.F., 2009. Comparison of ECVT and MR measurements of voidage in a gas-fluidized bed. Ind. Eng. Chem. Res. 48, 172–181. http://dx.doi.org/10.1021/ie8002073.

Makkawi, Y.T., Wright, P.C., 2002. Fluidization regimes in a conventional fluidized bed characterized by means of electrical capacitance tomography. Chem. Eng. Sci. 57, 2411–2437.

Makkawi, Y.T., Wright, P.C., 2004. Electrical capacitance tomography for conventional fluidized bed measurements—remarks on the measuring technique. Powder Technol. 148, 142–157. http://dx.doi.org/10.1016/j.powtec.2004.09.006.

Michailovich, O. V, 2011. An iterative shrinkage approach to total-variation image restoration. IEEE Trans. Image Process 20, 1281–1299. http://dx.doi.org/10.1109/TIP.2010.2090532.

Müller, C.R., Davidson, J.F., Dennis, J.S., Fennell, P.S., Gladden, L.F., Hayhurst, A.N., Mantle, M.D., Rees, A.C., Sederman, A.J., 2007a. Rise velocities of bubbles and slugs in gas-fluidised beds: ultra-fast magnetic resonance imaging. Chem. Eng. Sci. 62, 82–93. http://dx.doi.org/10.1016/j.ces.2006.08.019.

Müller, C.R., Davidson, J.F., Dennis, J.S., Gladden, L.F., Fennell, P.S., Hayhurst, A.N., Mantle, M.D., Rees, A.C., Sederman, A.J., 2007b. Oscillations in gas-fluidized beds: ultra-fast magnetic resonance imaging and pressure sensor measurements. Powder Technol. 177, 87–98. http://dx.doi.org/10.1016/j.powtec.2007.02.010.

Müller, C.R., Holland, D.J., Gladden, L.F., Davidson, J.F., Dennis, J.S., Hayhurst, A.N., Mantle, M.D., Sederman, A.J., 2007c. Rapid two-dimensional imaging of bubbles and slugs in a three-dimensional, gas-solid, two-phase flow system using ultrafast magnetic resonance. Phys. Rev. E 75, 020302. http://dx.doi.org/10.1103/PhysRevE.75.020302.

Peng, L., Merkus, H., Scarlett, B., 2000. Using regularization methods for image reconstruction of electrical capacitance tomography. Part. Part. Syst. Characterisation 17, 96–104.

Pore, M., Chandrasekera, T.C., Holland, D.J., Wang, A., Wang, F., Marashdeh, Q., Mantle, M.D., Sederman, A.J., Fan, L.-S., Gladden, L.F., Dennis, J.S., 2012. Magnetic resonance studies of jets in a gas–solid fluidised bed. Particuology 10, 161–169. http://dx.doi.org/10.1016/j.partic.2011.10.005.

Reinecke, N., Mewes, D., 1996. Recent developments and industrial/research applications of capacitance tomography. Meas. Sci. Technol. 7, 233–246.

Rowe, P.N., 1976. Prediction of bubble size in a gas fluidised bed. Chem. Eng. Sci. 31, 285–288. http://dx.doi.org/10.1016/0009-2509(76)85073-7.

Soleimani, M., Lionheart, W.R.B., 2005. Nonlinear image reconstruction for electrical capacitance tomography using experimental data. Meas. Sci. Technol. 16, 1987–1996. http://dx.doi.org/10.1088/0957-0233/16/10/014.

Tropp, J.A., Wright, S.J., 2010. Computational methods for sparse solution of linear inverse problems. Proc. IEEE 98, 948–958. http://dx.doi.org/10.1109/JPROC.2010.2044010.

Wang, H., Yang, W., Dyakowski, T., Liu, S., 2006. Study of bubbling and slugging fluidized beds by simulation and ECT. AIChE J 52, 3078–3087. http://dx.doi.org/10.1002/aic.

Wang, S., Dyakowski, T., Xie, C., Williams, R.A., Beck, M.S., 1995. Real time capacitance imaging of bubble formation at the distributor of a fluidized bed. Chem. Eng. J. 56, 95–100.

Wang, Y., Yang, J., Yin, W., Zhang, Y., 2008. A new alternating minimization algorithm for total variation image reconstruction. SIAM J. Imaging Sci 1, 248–272.

Warsito, W., Fan, L., 2001. Neural network based multicriteria optimization image reconstruction technique for imaging two- and three-phase flow systems using electrical capacitance tomography (ECT). Meas. Sci. Technol. 12, 2198–2210.

Werther, J., 1977. Zur Problematik der massstabsvergroesserung von wirbelschichtreaktoren. Chem. Ing. Tech 49, 777–785.

Xie, C.G., Huang, S.M., Hoyle, B.S., Thorn, R., Lenn, C., Snowden, D., Beck, M.S., 1992. Electrical capacitance tomography for flow imaging: system model for development of image reconstruction algorithms and design of primary sensors. IEEE Proc.-G 139, 89–98.

Yang, W., Peng, L., 2003. Image reconstruction algorithms for electrical capacitance tomography. Meas. Sci. Technol. 14, R1–R13.

Yang, W., Spink, D., York, T., McCann, H., 1999. An image-reconstruction algorithm based on Landweber's iteration method for electrical-capacitance tomography. Meas. Sci. Technol. 10, 1065–1069.